Journal of Materials Chemistry A

Accepted Manuscript

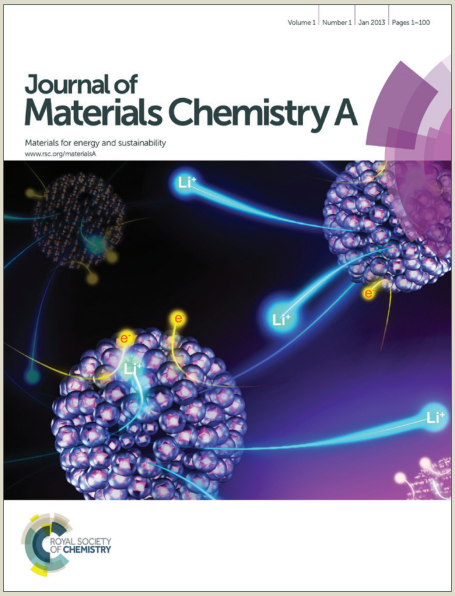

ROYAL SOCIETY OF CHEMISTRY

www.rsc.org/materialsA

Journal of Materials Chemistry A

Cite this: DOI: 10.1039/c0xx00000x

www.rsc.org/xxxxxx

ARTICLE TYPE

Improved Charge Transport of Nb-Doped TiO_2 Nanorods in Methylammonium Lead Iodide Bromide Perovskite Solar Cell

Mengjin Yang,[a] **Rui Guo,**[a] **Kamal Kadel,**[a] **Yunyan Liu,**[a,c] **Kevin O'Shea,**[b] **Richard Bone,**[a] **Xuewen Wang,**[a] **Jin He,**[a] **and Wenzhi Li,**[a,*]

Received (in XXX, XXX) Xth XXXXXXXXX 20XX, Accepted Xth XXXXXXXXX 20XX
DOI: 10.1039/b000000x

Nb-doped rutile nanorod-based methylammonium lead iodide bromide ($MAPbI_{3-x}Br_x$) perovskite solar cells have been developed by integrating an excellent photon-active perovskite sensitizer with the superior electron transporting rutile nanorods. It is found that there are two distinct stages in the formation of the perovskite materials prepared using non-stoichiometric mixed halide precursors, namely the orange colored bromine-rich transient state formed at 105 °C and the dark brown colored iodine-rich crystallized state formed at 155 °C. Optical, compositional, and crystalline properties of the perovskite samples at the two stages are studied by using UV/Vis spectroscopy, energy-dispersive x-ray spectroscopy, and x-ray diffraction. The mixed halide materials undergo a transition from an intermediate cubic phase to a well-crystallized tetragonal perovskite phase through complicated diffusion, evaporation, and intercalation processes. Furthermore, well-crystallized mixed halide perovskite is integrated with Nb-doped rutile nanorods and undoped rutile nanorods to fabricate perovskite solid state solar cells. Perovskite solar cells with Nb-doped rutile nanorods have significantly improved performance including increased short circuit current and open circuit voltage compared to perovskite solar cells with undoped rutile nanorods. The overall power conversion efficiency enhancement of the device with Nb-doped rutile nanorods is over 50 % compared with an undoped nanorod-based device , which is attributed to the superior charge collection efficiency of the Nb-doped rutile nanorods as evidenced by the electrochemical impedance measurement.

Introduction

The organo-metal halide perovskite solar cell has emerged as one of the most rapidly developing solar cells because of its high efficiency, low cost, and easy fabrication[1-5]. Within a short period of time, efficiency has been improved from 3.81 [6] to over 17%[7, 8]. The perovskite material, mainly composed of methylammonium lead trihalide ($MAPbX_3$), is a remarkable material for high efficiency solar cells because of its high extinction coefficient[9] and balanced long carriers transport length[10, 11]. The structure of the perovskite materials is intrinsically complex and rich[12]. The band gap[13], exciton binding energy[14], stability[13, 15], and charge transport property[10] can be tuned by mixing different halide perovoskite materials. Although several investigations have been conducted to unveil the structure of perovskite materials using different techniques, including Raman[16] and pair distribution function analysis[17], a comprehensive understanding of the process of perovskite formation, especially for mixed halides, is still lacking. Perovskite materials possess three different phases, namely orthorhombic, tetragonal, and cubic, for different temperature ranges[4]. For example, at room temperature, methylammonium lead iodide ($MAPbI_3$) has a tetragonal structure (I4/mcm) while methylammonium lead bromide ($MAPbBr_3$) has a cubic structure ($Pm\bar{3}m$). It has been reported that the structure and color of the perovskite can be tuned by adjusting the ratio of bromine to iodine in the perovskite material[13]. In this manuscript, we demonstrate that a mixed halide precursor with a non-stoichiometric ratio has a dramatic evolution in composition and structure during the baking process. The mixed halide precursors will transform from a cubic structure to a tetragonal structure with an increase of the temperature. The latter is suitable as an excellent sensitizer for solid state solar cells. Since the final performance of a perovskite solar cell is highly dependent on the process procedures of the perovskite materials[18-22], our finding about the dynamic formation of the perovskite materials provides valuable information and insight for the development of high efficient perovskite solar cells.

Another goal of this work is to improve the efficiency of perovskite solar cells by including Nb-doped rutile nanorods in the photoanode. The current perovskite solar cells involve two different structures, one mesoporous and the other planar. The planar structured perovskite solar cell requires the perovskite to have a long charge diffusion length comparable to its optical absorption length. For example, methylammonium lead iodide chloride ($MAPbI_xCl_{3-x}$) is a typical perovskite material which fulfils this requirement[23, 24]. Although the planar structure reduces the complexity of the structure and requires a simple process for the solar cell construction, difficulties in controlling the morphology and coverage of the perovskite film must be considered[25]. In contrast to the planar structure, the mesoporous photoanode-based perovskite solar cell allows control over the perovskite material loading. However, the conventional mesoporous perovskite solar cell is based on a functional nanoparticle layer, where slow charge transport inside the percolated nanoparticle network is dominant. Different approaches have been investigated to improve the electron transport/collection efficiency, such as insulating Al_2O_3 nanoparticle[15], ZnO nanoparticle[26], TiO_2/graphene composite[27], and one dimensional (1D) nanowire/nanorods [28-30]. Due to their superior charge transport, 1D materials have been studied as an alternative to particulate nanomaterials since the dye-sensitized solar cell era [31-33], but their performance is inferior to its nanoparticle counterpart due to the reduced surface area[34, 35]. Because the superior charge transport of nanowires has improved the efficiency of quantum dot solar cells[36, 37], it is expected that perovskite materials with high extinction coefficient will provide an opportunity to fully use the superior transport properties of the 1D materials. Although 1D materials provide the opportunity to adopt a thick layer of perovskite in perovskite solar cells [38], more work is required to understand how the electron transport property of the 1D materials will affect the performance of the perovskite solar cells. In this work, we demonstrate the effect of Nb-doped rutile nanorods on solar cell performance.

Experimental

Methylammonium lead iodide bromide ($MAPbI_xBr_{3-x}$) was synthesized as an analogue to methylammonium lead iodide chloride ($MAPbI_xCl_{3-x}$)[15]. First, 5 ml methylammine (33 wt% in pure ethanol, Sigma-Aldrich) was mixed with 25 ml pure ethanol (200 proof, Fisher) in a two-neck flask under a nitrogen atmosphere and ice bath, and then 2.5 ml hydroiodic acid (57 wt% in H_2O, Sigma-Aldrich) was injected into the excessive methylamine solution (2.1:1 molar ratio of methylamine to hydroiodic acid). The mixture was vigorously stirred in an ice bath for 2 hrs. The resulting solution was then transferred into a rotary evaporator and evaporated at 55 °C for about 4 hours until crystalline methylammonium iodide (MAI) was formed. A light yellowish powder was collected and cleaned with diethyl ether several times to remove excessive chemicals and further dried overnight in a vacuum oven (200 Torr) at room temperature. The perovskite precursor was prepared by dissolving MAI and $PbBr_2$ (99.8 %, Sigma-Aldrich) with 3:1 molar ratio in anhydrous N,N-dimethylformamide (99.8 %, Sigma-Aldrich), and the concentration of perovskite precursor ($MAPbI_{3-x}Br_x$) is around 0.7 M.

The method of growing TiO_2 nanorods on fluorine-doped tin oxide (FTO) was a slightly modified method reported elsewhere[35, 39]. Briefly, FTO substrate was cleaned by sonication in an acetone/isopropanol/DI water (1:1:1) solution for 15 min. A thin TiO_2 blocking layer was spin-coated (2000 rpm, 55 s) on FTO using 0.15 M titanium diisopropoxide bis(acetylacetonate) (75wt % in isopropanol, Sigma-Aldrich) in 1-butanol solution (99.4 %, Fisher), and was annealed in air at 450 °C for 30 min. Then the FTO substrate was patterned by the etching process of zinc powder (97 %, Fisher) with 2 M HCl solution[15]. After cleaning, the FTO was coated with the second blocking layer formed by spin coating (2000 rpm, 55 s) titanium tetraisopropoxide (TTIP) ethanolic acid solution as described in the previous paper[35]. The second blocking layer was fully crystallized after a 500 °C air annealing for 1hr. Nanorod growth on coated FTO took place with the mixture of saturated HCl (19 ml, 36.5-38 %, Fisher), H_2O (17 ml), and TTIP (0.5ml, 97 %, Sigma-Aldrich) in a Teflon-lined autoclave at 180°C for three hours. In the case of synthesizing Nb-doped doped rutile nanorods, additional 0.2 % (molar ratio) $NbCl_5$ (99.8 %, Acros Organics) with respect to TTIP was premixed with a hydrochloric acid solution overnight.

The solar cell device fabrication was conducted inside a nitrogen-filled glovebox with a relative humidity below 15 %. A perovskite layer was spin-coated on top of nanorods at 2500 rpm for 60s using the above mentioned perovskite precursor solution. The perovskite precursor-coated substrate was put aside at room temperature for 15 min before it was transferred onto a hotplate for baking. Two different temperatures were used for the baking, 105 °C and 155 °C. Then, a hole conducting polymer solution formed by mixing Spiro-OMeTAD (99 %, Richem International, 65 mM), tert-butylpyridine (TBP, 96 %, Sigma-Aldrich,19.5 mM), and lithium bis(trifluomethylsulfonyl) imide salt (Li-TFSI, 99 %, Acros Organics, 37.6 mM) in chlorobenzene (99.8 %, Acros Organics) was spin-coated on top of the perovskite layer at 2500 rpm for 60 s to form an electrolyte layer. Samples were left inside a desiccator overnight for oxygen doping, and a gold layer (100 nm) was deposited using an e-beam evaporator on top of the hole conducting layer to seal the device.

The morphology of the nanorods and device was observed by a field emission scanning electron microscope (FE-

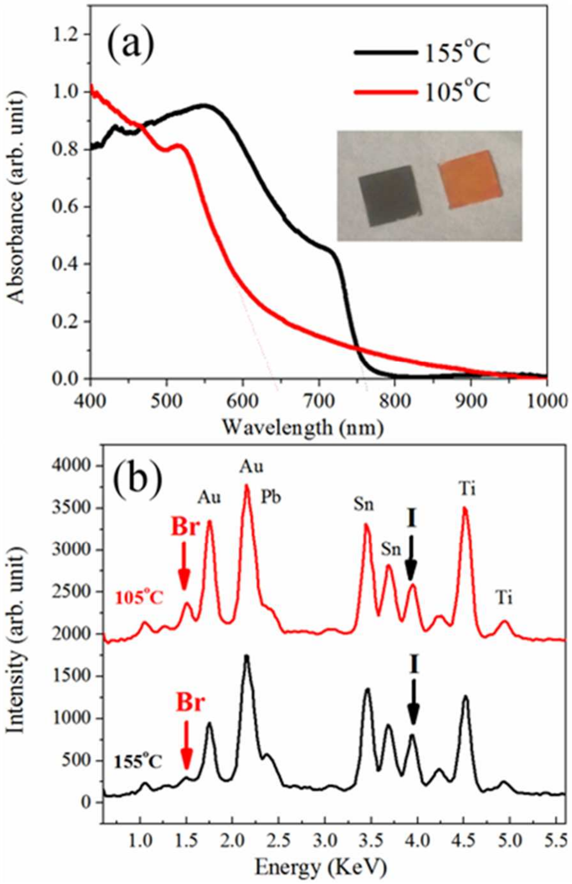

Figure 1, (a) Absorbance spectra of perovskite materials on top of glass slide baked at different temperatures, inset shows a photograph of the two samples baked at 105 °C (orange color) and 155°C (black color); (b) The EDS spectra of the two states of $MAPbI_{3-x}Br_x$ in assembled devices, read curve for sample baked at 105 °C and black curve for sample baked at 155 °C.

SEM, JEOL 6335F). Optical properties and a Raman spectrum of the perovskite film were characterized using a UV/Vis spectrometer (Ocean Optics, USB2000) and a Raman spectrometer (Renishaw Invia). Crystal structure analysis of the perovskite film was carried out by an X-ray diffractometer (Siemens D5000) with a Cu K1-α source. The I-V curve of the device was measured by a source meter (Keithley 2400) under AM 1.5 condition from a solar simulator (New Port). Incident photon-to-current efficiency (IPCE) was characterized by QEX10 solar cell quantum efficiency measurement system. Electrochemical impedance spectroscopy was conducted by a potentiostat (CHI 760D) at 10 mV alternating voltage from 0.1 Hz to 100 KHz with different forward biases under light illumination condition.

Results and discussion

The structure and optical properties of the perovskite materials are strongly dependent on their processing conditions. In the mixed halide perovskite material, there are two distinct states formed under different baking processes. At a relatively high baking temperature (155 °C), perovskite materials change color from light yellow to orange and eventually turn to a black or dark brown color within 15 minutes. At a lower temperature condition (105 °C) , the orange stage is relatively stable for a long time (more than a half hour). An optical photograph of the two different states is shown in the inset of Figure 1 (a). The different colors are indicators of the formation of the different structures of the crystalline perovskite from its precursor. Figure 1 (a) presents the absorption spectra of the perovskite materials formed at low temperature 105 °C (red curve) and high temperature 155 °C (black curve). The absorption edge of the perovskite material has shifted from 640 to 758 nm when the baking temperature of perovskite samples is increased from 105 to 155 °C . It is reported that pure $MAPbI_3$ and $MAPbBr_3$ perovskite materials have up-absorption limits of 800 nm and 520 nm, respectively[6]. Our results fall between the two boundaries of the absorption edges of the pure $MAPbI_3$ and $MAPbBr_3$ phases, and agree well with the reported mixed halide systems[13, 28]. It should be noted that there are two peaks for the perovskite material baked at 155 °C. The two peaks may come from the absorption between two separate valence bands (VB1, VB2) and the common conduction band.[11] The absorption edge shift towards a longer wavelength with the increase of the baking temperature may indicate the change of the constituents in the perovskite material during the crystallization process. Figure 1 (b) shows the energy dispersive x-ray (EDS) of the perovskite materials obtained at low (105 °C) and high (155 °C) temperatures. It can be seen that the ratio of Br peak to I peak (Br/I) has reduced from sample processed at 105 °C (1.3) to sample processed at 155 °C (0.1) in the EDS spectra. The key structure of the perovskite is the octahedron (PbX_6, lead surrounded by 6 halides). It has been reported that lead salt would form a complex in DMF solution.[40, 41] $PbI_2{\cdot}DMF$ with a core structure $[PbI_6]^{4-}$ octahedra is formed for PbI_2 in DMF solution[42], and similar structure $[PbBr_6]^{4-}$ octahedra is expected for $PbBr_2$ DMF solution. The original ratio of Br/I in the precursor is 2/3, and the formation of octahedron of PbX_6 during the baking will have a higher concentration of Br at the beginning due to the use of $PbBr_2$. As the heating proceeds, the organic component will be lost[21], and bromine ions will be replaced by the diffusion of iodine ions so that Br/I is reduced. Fig. S1 gives the Raman spectra of the two samples baked at different temperatures. Peaks in the Raman can be assigned to libration and torsional modes of methylammonium cations[16]. The power used to measure Raman for sample baked at 155 °C is two orders higher than for sample baked at 105 °C, indicating the significant loss of the methylammonium cation during the baking process. It is a complex process with a loss of the organic component and diffusion of different ions.

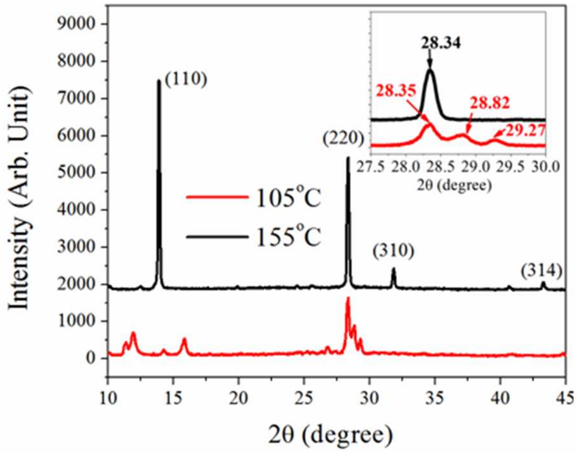

Figure 2, XRD patterns of the perovskite materials formed at different temperatures (105°C, red curve) and (155°C, black curve) on glass slide substrates. Inset shows the zoom-in pattern between 27.5° and 30°.

XRD was used to characterize the crystal phases of the perovskite materials processed at different baking temperatures, as shown in Figure 2. At the high temperature (155°C), the perovskite material has sharp peaks in its XRD profile (black cure in Figure 2) indicating the formation of well crystallized tetragonal perovskite. The peaks at 13.92, 28.35, 31.82, 43.30 ° can be assigned to (110), (220), (310), and (314) respectively based on the previously reported data[43]. For tetragonal perovskite, there are normally a few peaks that overlap with each other, such as (002)/(110), (004)/(220), (411)/(314) [12, 44]. For the low temperature (105 °C) baked sample, the peaks of the perovskite are wider and weaker (see red curve in Figure 2). More importantly, there are some strong unidentified peaks (11.3, 11.9, and 15.9 °) surrounding the major peaks. Those unidentified peaks may come from the product formed due to the slow drying process in the presence of water (lead oxyhalides)[45] or the intermediate states[46]. As shown in the inset of Figure 2, there are three peaks (28.35, 28.82, and 29.27 °) for low temperature baked perovskite while only one peak (28.34°) for the high temperature baked perovskite in the range of 28-29.5 °. Perovskite processed at low temperature has mixed phases (tetragonal and cubic), and it was fully converted to the tetragonal phase at high temperature, based on previous XRD study in mixed bromide/iodide perovskite[13].

In the perovskite precursor, non-stoichiometric ratio of MAI to $PbBr_2$ is used because higher amount of MAI will compensate the loss of MAI during the baking process. It is also found that higher $MAI/PbBr_2$ ratio results in slower crystallization process. As shown in the XRD profiles in Fig. S2, at a low MAI/$PbBr_2$ ratio, perovskite phase (as indicated by the peak at~14°) forms quickly, and a lead iodide phase (as indicated by the peak at 12.6°) emerges if the precursor is baked for a long time. At high MAI/$PbBr_2$ ratio, it takes a longer time to reach crystallized perovskite, which agrees with the reported long annealing time for other methylammonium halide additives[46]. The morphologies of rutile nanorods with and without Nb doping are examined by scanning electron microscopy (SEM) as shown in Figure 3. The undoped nanorod has a diameter of around 45 nm while 0.20% Nb-doped nanorod has a diameter of about 55 nm. The diameter increase in the Nb-doped nanorod is attributed to the suppression of anisotropic growth of rutile nanorods by Nb doping. The surface energy difference is reduced with Nb doping so that the driving force of anisotropic growth is decreased as reported previously[39, 47]. The cross-section view, as shown in the insets in Figure 3, shows that the length of the undoped and Nb-doped doped nanorods is around 520 nm, indicating that the small amount of Nb doping will not affect very much the growth length of the nanorods.

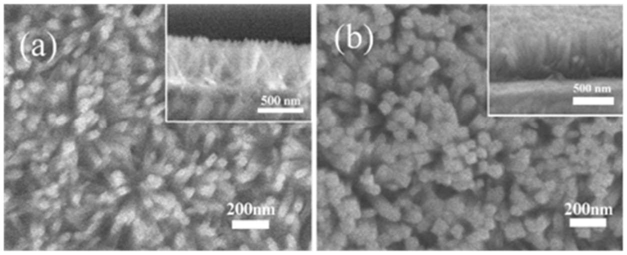

Figure 3, SEM diagram of pure nanorods (a) and 0.2% Nb-doped nanorods (b). The insets show the cross-sectional view of the two samples.

The fabrication procedures of the nanorod-based perovskite solar cell are described in detail in the experimental section. A schematic of the device is shown in Figure 4 (a), and a cross-sectional SEM diagram of an actual device consisting of undoped nanorods is shown in Figure 4 (b). The cross-sectional SEM image (Figure 4(b)) confirms the designed configuration. The nanorods with a length of 500 nm are grown on a TiO_2 blocking layer coated on FTO, and the perovskite material is embedded between the vertically aligned nanorods. Hole transport material (HTM, Spiro-OMeTAD) is formed on the top of the perovskite material, and a gold layer is deposited on the hole transport material to form the back electrode. The thickness of nanorods with perovskite, the overlayer of HTM, and gold layer are 510 nm, 375 nm, and 100 nm respectively.

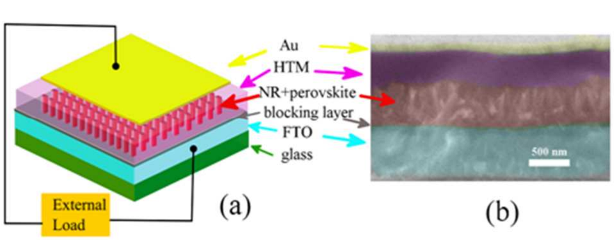

Figure 4, (a) A schematic of nanorod based perovskite solar cells, and (b) a cross-sectional SEM image of an actual perovskite solar cell (artificial colors are used to distinguish different layers).

The performance of the perovskite champion solar cells made of different nanorods is shown in Figure 5. Nb doping to rutile nanorods has a dramatic effect on the performance of the solar cell. As shown in Figure 5, the short-circuit current has increased from 11.68 mA/cm^2 of solar cells consisting of undoped nanorods (black curve) to 16.50 mA/cm^2 for solar cells consisting of 0.2% Nb-doped nanorods (red curve), and the open-circuit voltage has been improved from 0.83 V in an undopednanorod solar cell to 0.87 V in an Nb-doped nanorod cell. The fill factor for solar cells fabricated using undoped nanorods and 0.2% Nb-doped nanorods is almost the same (0.52); however the power conversion efficiency has increased from 4.9% for undoped nanorod solar cell to 7.5% for 0.2% Nb-doped nanorod solar cell, which is a 50% increase. The reproducibility of the devices was surveyed in the supplemental materials, and a similar substantial boost of efficiency after Nb doping has been observed. The extinction spectra (Fig. S4) of perovskite films formed on NR and Nb-doped NR are very similar, but the IPCE shows higher quantum efficiency after Nb doping. Nb-doped TiO_2 has been reported to be superior to plain TiO_2 due to several reasons. For example, the flat band of TiO_2 after Nb doping will be positively shifted so that electron injection is more energetically favorable. [39, 48] Nb doping can also improve the electron transport and collection by providing high conductive path and better interface contact.[39, 49]. Transmission electron microscope EDS of Nb-doped nanorod shows the doping of Nb inside nanorod (Fig. S5) which is beneficial for improving the aforementioned charge dynamics (such as electron injection, transport, and collection) and therefore enhances the solar cell's performance. Electrochemical impedance spectroscopy (EIS) was

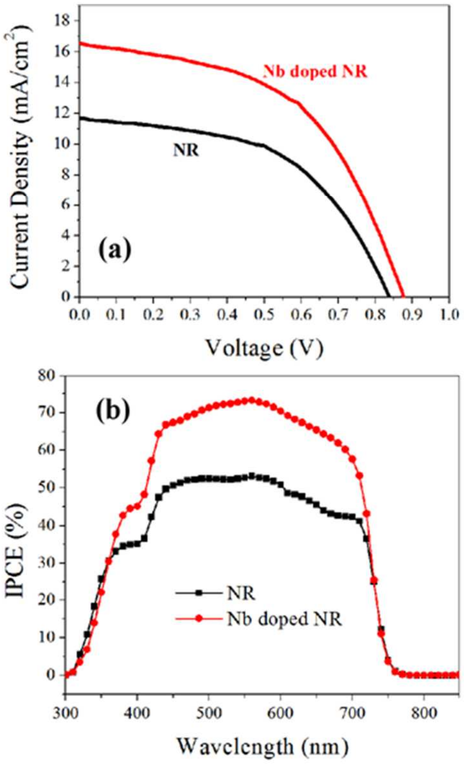

Figure 5, J-V curves (a) and IPCE (b) of the perovskite solar cells made of pure nanorods (black curve) and 0.2% Nb-doped nanorods.

employed to confirm the charge transport dynamics in Nb-doped doped nanorods based device.

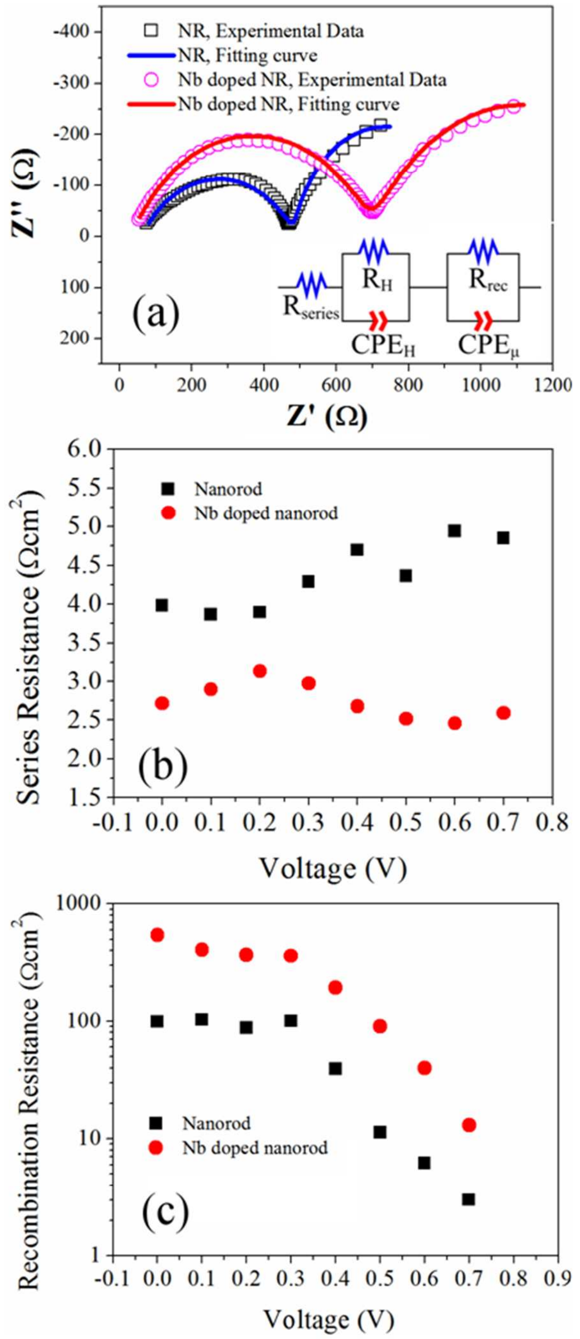

Figure 6, (a) Nyquist plot of solar cells fabricated using pure NRs and Nb-doped NRs at 0.4 V forward bias, inset is the equivalent circuit used to fit the experimental data, (b) series resistance of devices at different biases, and (c) recombination resistance of devices at different biases.

. EIS is a very powerful technique to reveal the underlying carrier transport behavior in perovskite solar cells[50-52]. Typical impedance spectra of undoped nanorods and Nb-doped nanorod-based devices are shown in Figure 6 (a). There are two semicircles in the Nyquist plot; the one on the left side corresponding to high frequency comes from the hole transport in spiro-OMeTAD, and the other one on the right side corresponding to low frequency is related to the electron transport in the photoanode (including interfaces between photoanode and HTM), which can be described either by a classic transmission line model or Gerischer element[52]. The equivalent circuit to fit the experimental data is shown in the inset of Figure 6 (a). Basically, a series resistance (R_{series}) is in series with two RC elements. One RC element (R_H, CPE_H) is related to the hole transport in spiro-OMeTAD, and the other one represents the recombination resistance (R_{rec}) and chemical capacitance (CPE_μ) on the photoanode side. The fitted R_{series} and R_{rec} are plotted with respect to applied forward biases as shown in Figure 6 (b) and (c). The value of R_{series} in the Nb-doped nanorod-based device decreases to 2.7 Ωcm^2 on average compared to 4.3 Ωcm^2 in the pure nanorod-based device, while R_{rec} in the device made from Nb-doped nanorods increases more than three times that in the undoped nanorod- based device. EIS data show clearly the improved electron transport and reduced recombination in Nb-doped nanorods. This result indicates that the Nb doping can boost electron collection efficiency in the solar cells. This result agrees well with other higher electron collecting systems (graphene/TiO_2) [53] .

Conclusions

A non-stoichiometric mixed halide precursor (iodide and bromide) with excess methylammonium iodide shows two distinct stages at different baking temperatures. An orange colored bromine rich perovskite with cubic/tetragonal phase was formed at 105 °C, and it was converted to dark brown colored iodine rich perovskite with pure tetragonal phase after 155 °C baking. Solar cells fabricated by embedding rutile nanorods doped with 0.2% Nb by mixed halide baked at high temperature (155 °C) showed an efficiency of 7.5% which is a 50% increase in the efficiency (4.9%) of solar cells fabricated using undoped rutile nanorods. It is found that lower series resistance and higher recombination resistance resulting from the Nb doping contribute to significant improvement of the solar cell performance.

Acknowledgement:

This work is supported by the American Chemical Society Petroleum Research Foundation under grant 51766-ND10. We are grateful to Dr. Gaohui Du and Dr. Qingmei Su for their help with the TEM EDS work. We acknowledge the use of the SEM and XRD at the AMERI at Florida International University.

Notes and references

[a] *Department of Physics, Florida International University, Miami, FL 33199, United States*
[b] *Department of Chemistry and Biochemistry, Florida International University, Miami, FL, 33199, United States*
[c] *Permanent address: Department of Optics Information Science and Technology, School of Sciences, Shandong University of Technology, Zibo, Shandong Province 255049, P.R. China*

[*] *Corresponding author: wenzhi.li@fiu.edu*
† Electronic Supplementary Information (ESI) available: Raman spectra of perovskite. See DOI: 10.1039/b000000x/
.

References

1. N.-G. Park, *J. Phys. Chem. Lett.*, 2013, **4**, 2423-2429.
2. H. J. Snaith, *J. Phys. Chem. Lett.*, 2013, **4**, 3623-3630.
3. P. P. Boix, K. Nonomura, N. Mathews and S. G. Mhaisalkar, *Mater. Today*, 2014, **17**, 16-23.
4. H.-S. Kim, S. H. Im and N.-G. Park, *J. Phys. Chem. C*, 2014, **118**, 5615-5625.
5. S. Kazim, M. K. Nazeeruddin, M. Grätzel and S. Ahmad, *Angew. Chem. Int. Ed.*, 2014, **53**, 2812-2824.
6. A. Kojima, K. Teshima, Y. Shirai and T. Miyasaka, *J. Am. Chem. Soc.*, 2009, **131**, 6050-6051.
7. NREL, Research Cell Efficiency Records, http://www.nrel.gov/ncpv/images/efficiency_chart.jpg, (accessed May 2014).
8. R. F. Service, *Science*, 2014, **344**, 458.
9. H.-S. Kim, C.-R. Lee, J.-H. Im, K.-B. Lee, T. Moehl, A. Marchioro, S.-J. Moon, R. Humphry-Baker, J.-H. Yum, J. E. Moser, M. Gratzel and N.-G. Park, *Sci. Rep.*, 2012, **2**, 591.
10. S. D. Stranks, G. E. Eperon, G. Grancini, C. Menelaou, M. J. P. Alcocer, T. Leijtens, L. M. Herz, A. Petrozza and H. J. Snaith, *Science*, 2013, **342**, 341-344.
11. G. Xing, N. Mathews, S. Sun, S. S. Lim, Y. M. Lam, M. Grätzel, S. Mhaisalkar and T. C. Sum, *Science*, 2013, **342**, 344-347.
12. T. Baikie, Y. N. Fang, J. M. Kadro, M. Schreyer, F. X. Wei, S. G. Mhaisalkar, M. Graetzel and T. J. White, *J Mater Chem A*, 2013, **1**, 5628-5641.
13. J. H. Noh, S. H. Im, J. H. Heo, T. N. Mandal and S. I. Seok, *Nano Lett.*, 2013, **13**, 1764–1769.
14. N. Kitazawa, Y. Watanabe and Y. Nakamura, *J Mater Sci*, 2002, **37**, 3585-3587.
15. M. M. Lee, J. Teuscher, T. Miyasaka, T. N. Murakami and H. J. Snaith, *Science*, 2012, **338**, 643-647.
16. C. Quarti, G. Grancini, E. Mosconi, P. Bruno, J. M. Ball, M. M. Lee, H. J. Snaith, A. Petrozza and F. D. Angelis, *J. Phys. Chem. Lett.*, 2014, **5**, 279-284.
17. J. J. Choi, X. H. Yang, Z. M. Norman, S. J. L. Billinge and J. S. Owen, *Nano Lett.*, 2014, **14**, 127-133.
18. J. Burschka, N. Pellet, S.-J. Moon, R. Humphry-Baker, P. Gao, M. K. Nazeeruddin and M. Gratzel, *Nature*, 2013, **499**, 316-319.
19. M. Z. Liu, M. B. Johnston and H. J. Snaith, *Nature*, 2013, **501**, 395-398.
20. Q. Chen, H. Zhou, Z. Hong, S. Luo, H.-S. Duan, H.-H. Wang, Y. Liu, G. Li and Y. Yang, *J. Am. Chem. Soc.*, 2014, **136**, 622-625.
21. C. Wehrenfennig, G. E. Eperon, M. B. Johnston, H. J. Snaith and L. M. Herz, *Adv. Mater.*, 2014, **26**, 1584-1589.
22. J. Y. Jeng, Y. F. Chiang, M. H. Lee, S. R. Peng, T. F. Guo, P. Chen and T. C. Wen, *Adv. Mater.*, 2013, **25**, 3727-3732.
23. P. Docampo, J. M. Ball, M. Darwich, G. E. Eperon and H. J. Snaith, *Nat Commun*, 2013, **4**, 2761.
24. J. B. You, Z. R. Hong, Y. Yang, Q. Chen, M. Cai, T.-B. Song, C.-C. Chen, S. R. Lu, Y. S. Liu, H. P. Zhou and Y. Yang, *Acs Nano*, 2014, **8**, 1674-1680.
25. G. E. Eperon, V. M. Burlakov, P. Docampo, A. Goriely and H. J. Snaith, *Adv. Funct. Mater.*, 2014, **24**, 151-157.
26. D. Liu and T. L. Kelly, *Nat Photon*, 2014, **8**, 133-138.
27. J. T.-W. Wang, J. M. Ball, E. M. Barea, A. Abate, J. A. Alexander-Webber, J. Huang, M. Saliba, I. Mora-Sero, J. Bisquert, H. J. Snaith and R. J. Nicholas, *Nano Lett.*, 2014, **14**, 724-730.
28. J. H. Qiu, Y. C. Qiu, K. Y. Yan, M. Zhong, C. Mu, H. Yan and S. H. Yang, *Nanoscale*, 2013, **5**, 3245-3248.
29. D. Bi, G. Boschloo, S. Schwarzmuller, L. Yang, E. M. J. Johansson and A. Hagfeldt, *Nanoscale*, 2013, **5**, 11686-11691.
30. H.-S. Kim, J.-W. Lee, N. Yantara, P. P. Boix, S. A. Kulkarni, S. Mhaisalkar, M. Grätzel and N.-G. Park, *Nano Lett.*, 2013, **13**, 2412-2417.
31. M. Law, L. E. Greene, J. C. Johnson, R. Saykally and P. D. Yang, *Nat. Mater.*, 2005, **4**, 455-459.
32. M. J. Yang, B. Ding, S. Lee and J. K. Lee, *J. Phys. Chem. C*, 2011, **115**, 14534-14541.
33. X. Feng, K. Zhu, A. J. Frank, C. A. Grimes and T. E. Mallouk, *Angew. Chem. Int. Ed.*, 2012, **51**, 2727-2730.
34. J. B. Baxter and E. S. Aydil, *Appl. Phys. Lett.*, 2005, **86**, 053114.
35. M. J. Yang, S. Neupane, X. W. Wang, J. He, W. Z. Li and N. Pala, *ACS Appl. Mater. Interfaces*, 2013, **5**, 9809-9815.
36. X. z. Lan, J. Bai, S. Masala, S. M. Thon, Y. Ren, I. J. Kramer, S. Hoogland, A. Simchi, G. I. Koleilat, D. Paz-Soldan, Z. j. Ning, A. J. Labelle, J. Y. Kim, G. Jabbour and E. H. Sargent, *Adv. Mater.*, 2013, **25**, 1769-1773.
37. Z. Ning, D. Zhitomirsky, V. Adinolfi, B. Sutherland, J. Xu, O. Voznyy, P. Maraghechi, X. Lan, S. Hoogland, Y. Ren and E. H. Sargent, *Adv. Mater.*, 2013, **25**, 1719-1723.
38. D.-Y. Son, J.-H. Im, H.-S. Kim and N.-G. Park, *J. Phys. Chem. C*, 2014, ASAP.
39. M. J. Yang, B. Ding and J.-K. Lee, *J. Power Sources*, 2014, **245**, 301-307.
40. I. Persson, K. Lyczko, D. Lundberg, L. Eriksson and A. Płaczek, *Inorg. Chem.*, 2011, **50**, 1058-1072.

41. A. Wakamiya, M. Endo, T. Sasamori, N. Tokitoh, Y. Ogomi, S. Hayase and Y. Murata, *Chem. Lett.*, 2014, **43**, 711-713.
42. Q. Wang, J.-H. Yun, M. Zhang, H. Chen, Z.-G. Chen and L. Wang, *J Mater Chem A*, 2014, **2**, 10355-10358.
43. Y. X. Zhao and K. Zhu, *J. Phys. Chem. Lett.*, 2013, **4**, 2880-2884.
44. K. N. Liang, D. B. Mitzi and M. T. Prikas, *Chem. Mater.*, 1998, **10**, 403-411.
45. A. Dualeh, N. Tétreault, T. Moehl, P. Gao, M. K. Nazeeruddin and M. Grätzel, *Adv. Funct. Mater.*, 2014, Early View.
46. Y. X. Zhao and K. Zhu, *J. Phys. Chem. C*, 2014, **118**, 9412-9418.
47. Y. Pang and P. Wynblatt, *J. Am. Ceram. Soc.*, 2006, **89**, 666-671.
48. X. J. Lu, X. L. Mou, J. J. Wu, D. W. Zhang, L. L. Zhang, F. Q. Huang, F. F. Xu and S. M. Huang, *Adv. Funct. Mater.*, 2010, **20**, 509-515.
49. S. Lee, J. H. Noh, H. S. Han, D. K. Yim, D. H. Kim, J. K. Lee, J. Y. Kim, H. S. Jung and K. S. Hong, *J. Phys. Chem. C*, 2009, **113**, 6878-6882.
50. A. Dualeh, T. Moehl, N. Tétreault, J. Teuscher, P. Gao, M. K. Nazeeruddin and M. Grätzel, *Acs Nano*, 2014, **8**, 362-373.
51. E. J. Juarez-Perez, M. Wuβler, F. Fabregat-Santiago, K. Lakus-Wollny, E. Mankel, T. Mayer, W. Jaegermann and I. Mora-Sero, *J. Phys. Chem. Lett.*, 2014, **5**, 680-685.
52. V. Gonzalez-Pedro, E. J. Juarez-Perez, W.-S. Arsyad, E. M. Barea, F. Fabregat-Santiago, I. Mora-Sero and J. Bisquert, *Nano Lett.*, 2014, **14**, 888-893.
53. J. T. Wang, J. M. Ball, E. M. Barea, A. Abate, J. A. Alexander-Webber, J. Huang, M. Saliba, I. Mora-Sero, J. Bisquert, H. J. Snaith and R. J. Nicholas, *Nano Lett.*, 2014, **14**, 724-730.

Graphic Abastract